Atmospheric River and Precipitation: Climate Change and Land Surface Temperature Impact, 1995-2015

Jiawen Tang

ABSTRACT

Atmospheric rivers (ARs) were the focus of my study, as they are narrow corridors of water vapor transport that played a crucial role in delivering precipitation to the west coast of North America. Unlike tropical cyclones, ARs possessing relatively low energy but have significant socio-economic impacts through intense precipitation. Recent studies had identified a strong correlation between sea surface temperature (SST) and atmospheric water vapor content, which is a key factor in AR intensity ratings. Under climate change, land surface temperatures (LST) exhibited more pronounced fluctuations than SST, yet the implications of these changes on precipitation dynamics remained underexplored. I utilized the Atmospheric River Catalog SIO-R1 and the reanalysis model MERRA-2 to investigate the precipitation caused by landfalling ARs on North America's west coast from 1995 to 2015. I focused on how variations in LST influenced precipitation and the efficiency of water vapor conversion to precipitation. My findings revealed a marked seasonality in ARs, with peak precipitation intensities occurring at intermediate temperatures. There was a notable inconsistency between water vapor and precipitation in seasonal variation. During the rainy season, higher pre-precipitation LSTs were linked to an increased likelihood and intensity of extreme precipitation events, especially at higher latitudes. The intensity of extreme precipitation increased by over 7%/K, above the rate of increase in water vapor, highlighting the critical role of local LST in predicting precipitation from ARs. This research underscored the need for a more systematic investigation into the interplay between LST changes and precipitation conversion in the context of warming climates.

KEYWORDS

Extreme weather events, Water vapor transport, Temperature anomaly, Climate change, Atmospheric modeling

INTRODUCTION

According to the IPCC Summary for Policymakers, "It is unequivocal that human influence has warmed the atmosphere, ocean, and land" (Change (IPCC) 2023). Climate change has elevated the global average temperature, and due to the current energy imbalance on Earth, temperatures will continue to rise toward equilibrium even with immediate emission cessation (Hansen et al. 2011). In line with the Clausius-Clapeyron Relationship, elevating air temperature enhances the air's potential to hold water vapor. Specifically, for every 1 degree Celsius rise in temperature, the air's water content can increase by around 7% (Trenberth 2011). While greenhouse gas concentrations remain generally consistent throughout the atmosphere, discernible temperature and precipitation patterns emerge as a result of interactions between winds and ocean currents (Xie et al. 2010). As climate changes, temperature and precipitation distributions tend to expand, leading to more pronounced temporal and spatial variations.

The expansion in the rainfall distribution will give rise to heightened rainfall extremes. In the context of climate change, both the frequency and intensity of extreme rainfall events are projected to intensify (O'Gorman 2015). Situated along the U.S. West Coast, California experiences the influences of both Mediterranean climate and mid-latitudinal dynamics, and there have been documented increases in precipitation variability in twenty-first-century California (Swain et al. 2018). Based on observational data, California's rainfall patterns have experienced shifts and delays of up to a month (Luković et al. 2021). The consequences of climate change-induced extremes and alterations are heavily influenced by adaptation policies, with local soil and water management offering the potential to prevent and mitigate disasters (Ralph et al. 2019). Comprehensive rainfall prediction is essential for shaping adaptation strategies, and in California, atmospheric rivers represent a significant constituent of its precipitation patterns.

Atmospheric rivers (ARs), as defined by NOAA, represent narrow channels responsible for the transport of water vapor outside the tropical regions (Gimeno et al. 2014). The predominant model for AR is quantified and characterized using Integrated Water Vapor Transport (IVT) (Waliser and Cordeira 2020). Globally, ARs contribute to 22% of the total global runoff, with regions such as California contributing over 50% (Paltan et al. 2017). Currently, the physical mechanism behind the formation of ARs remains unclear, limiting our ability to predict these events in advance; instead, we can only observe and predict them on a small-scale basis after they

have occurred (Payne et al. 2020). Nevertheless, ARs significantly impact California's climate, with floods and subsequent secondary disasters exacerbating droughts and wildfires in the following years (Michaelis et al. 2022). As sea surface temperatures (SST) rise, there's an expected surge in IVT over the Northeast Pacific Ocean. The transformation of precipitation due to IVT is modulated by topography and AR direction (Payne et al. 2020). Yet, there's a research gap concerning AR-associated rainfall trends in the climate change paradigm, especially related to land surface temperature (LST).

In this study, I focused on identifying AR-induced precipitation trends along the west coast of North America during the period 1995-2015. The central research question is to determine how AR-induced precipitation is associated with LST and whether this can indicate potential extreme precipitation events. I started with examining the correlation between AR-induced precipitation and LST to look for potential associations. I analyzed the conversion ratio between IVT and precipitation and used the temperature before precipitation as the conditional variable for determining potential extreme precipitation. I then analyzed the data overtime, exploring the relationships between variables and interpreting and testing hypotheses for data associations. Since the changes in water vapor and precipitation is none linear to temperature, and I could not take topography into account in the calculation process, I focused on analyzing trends and the extent to which extreme weather occurs, rather than nonlinear theory. Finally, I conducted variable control of latitude to explore the change of the influence of different latitudes on the distribution. The analysis utilized AR data from the Catalog of landfalling atmospheric rivers along the western coast of North America (SIO-R1) generated based on NCEP Reanalysis (Gershunov et al. 2017). Temperature data and the calibration of precipitation data were using the Reanalysis Model MERRA-2 (Gelaro et al. 2017).

METHODS

Study site and Data

I analyzed the landfalling atmospheric river (AR) events from 1995 to 2015 that caused precipitation on the west coast of North America using data from SIO-R1 and MERRA-2. The "Catalog of landfalling atmospheric rivers along the western coast of North America" (SIO-R1) is a seven-decade-long catalog of landfalling ARs based on NCEP Reanalysis (Gershunov et al., 2017). This catalog compiles AR data at 6-hour intervals from 1948 to 2017, covering latitudes from 25 to 52.5 degrees north and longitudes from 100 to 125 degrees west. This range effectively encompasses the majority of the Eastern Pacific landfalling ARs, from their approach to the coast to their eventual landfall. The directory's NetCDF file stored detailed daily rainfall data under the AR footprint (IVT > 250 kg/m/s) with a spatial resolution of 6x6 km (Figure 1).

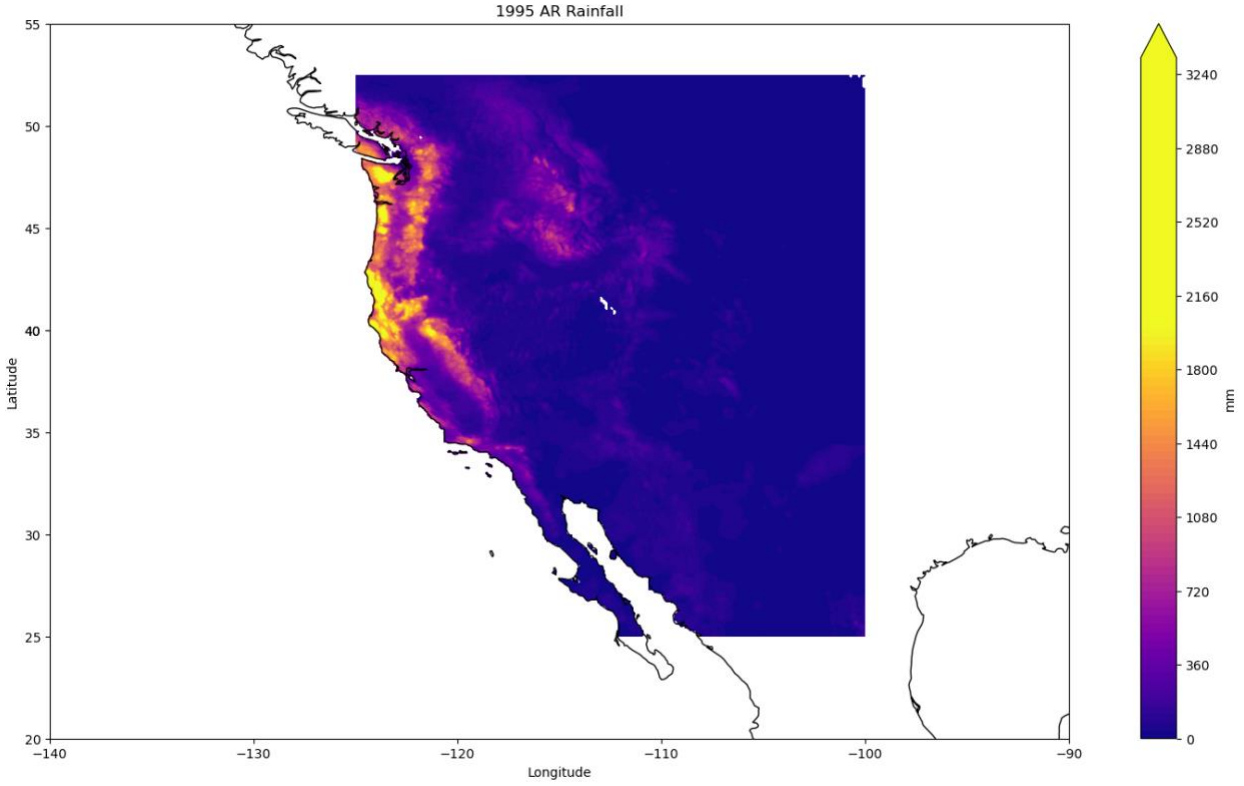

Figure 1. 1995 AR Precipitation Visualization from SIO-R1. This map displays the geographical distribution of AR-induced precipitation across the west coast of North America. X and Y axes represent longitude and latitude, respectively, with a continental base map. Colors indicate cumulative precipitation levels in millimeters for the year 1995, with a spatial resolution of 6 x 6 km.

For my temperature and rainfall data corrections, I used the Modern-Era Retrospective Analysis for Research and Applications, Version 2 (MERRA-2), which is the latest atmospheric reanalysis produced by NASA. MERRA-2 offers a resolution of 0.5° latitude by 0.625° longitude (Gelaro et al., 2017). The specific subset employed was MERRA-2 inst3_3d_asm_Np: 3d, 3-Hourly, Instantaneous, Pressure-Level, Assimilation, Assimilated Meteorological Fields V5.12.4 (M2I3NPASM), which provides instantaneous 3-dimensional data every three hours. The data covered the period from January 1, 1995, to December 31, 2015, except for December 31, 2012, which was missing due to leap year matching. The spatial coverage of the M2I3NPASM data extended globally from -180.0 to 180.0 degrees longitude and from -90.0 to 90.0 degrees latitude. I matched this data range with that of the SIO-R1 through location matching, ensuring that the final usage range was consistent with Figure 1. Given that the MERRA-2 data had a shorter time interval, I upscaled the data from 3-hour intervals to 6-hour intervals while maintaining the resolution at 0.5° x 0.625°. I corrected the IVT and precipitation values to address some inconsistencies in the model. Ultimately, I compiled a dataset of AR-induced precipitation events from 1995 to 2015, including variables such as location, IVT, precipitation, surface temperature, initial time, and duration (Table 1). All data were combined using ARID as the index, which is the number assigned to an event in the SIO-R1 catalog system. Each ARID is assigned a Date Number to prevent overlap, as the unique properties of ARs make simultaneous occurrences in my research area nearly impossible (Ryoo et al., 2015).

Table 1. Variables used in the analysis. This table lists the variables analyzed in the study, along with their respective units and data sources. Each variable is essential for understanding the dynamics of atmospheric rivers and their impact on precipitation patterns. The table includes information on integrated water vapor transport (IVT), atmospheric river identification (ARID), geographical location, precipitation amounts, time intervals, and surface temperature. Data sources are primarily from the SIO-R1 and M2I3NPASM databases. The data units have been upscaled and aggregated to match the resolution required for visualization and analysis. The resolutions are listed to ensure clarity on the granularity of the data used in the study.

Variable	Unit	Data Source	Resolution
IVT	kg/m/s	SIO-R1	6 x 6 km
ARID	/		0.5° x 0.625° (aggregated) Per event, 2795-4126
Location	degree	SIO-R1 Matched with M2I3NPASM	0.5° x 0.625°
Precipitation	mm		0.5° x 0.625° (aggregated)
Time	Hour	SIO-R1 M2I3NPASM upscaled	6 Hour Integrated
Surface Temperature	Kelvin	M2I3NPASM	0.5° x 0.625°

Atmospheric river methodology

Based on previous studies (Gimeno et al. 2014, Mundhenk et al. 2016), ARs are typically detected using two different spatial fields: some form of precipitable water (IWV) and some form of integrated water vapor transport (IVT). According to the recommendations of the AR Tracking Method Intercomparison Project (ARTMIP) (Shields et al., 2023), the current mainstream AR Catalog tier 2 primarily utilizes IVT as its main algorithm. IVT is defined as:

$$\mathrm{IVT} = \sqrt{\left(\frac{1}{g}\int_{1000\mathrm{hPa}}^{300\mathrm{hPa}} q\,u\,dp\right)^2 + \left(\frac{1}{g}\int_{1000\mathrm{hPa}}^{300\mathrm{hPa}} q\,v\,dp\right)^2}$$

IVT is calculated using the formula where g represents gravitational acceleration, q is specific humidity, u is zonal wind, v is meridional wind, and dp is the pressure difference between adjacent pressure levels (Mundhenk et al. 2016). The mass-weighted vertical integration of these components is performed using data from 1000 to 300 hPa, and the wind data is at 850 hPa. An IVT value greater than 250 kg/m/s is considered a general footprint of ARs, and the SIO-R1 model has demonstrated that all ARs meet this criterion (Lavers & Villarini, 2013; Gershunov et al., 2017). Since the purpose of my research is not to identify ARs, I will rely on and use the ARs cataloged by SIO-R1. AR intensity and categorization systems utilize Max IVT and duration as indices (Ralph et al., 2019). In this study, I will examine whether maximum IVT can serve as an effective indicator of AR impact.

Climatology and variability

The climatology of AR landfalls from 1995 to 2015 primarily focuses on frequency and seasonality. Detailed analyses regarding intensity, duration, and location of occurrence have been addressed in prior research (Gershunov et al., 2017). In the study area, the proportion of AR-induced precipitation reaches 65% in coastal regions and 30% in inland areas, both of which exceed the global averages of 50% and 22%, respectively (Paltan et al., 2017). For regional classification, the areas I examined are designated as Western North America (WNA), Northern Central America (NCA), Central North America (CAN), and the principal coastal areas of the

North Pacific Ocean (NPO) according to the IPCC's updated climate zones (Iturbide et al., 2020). These regions are relatively understudied compared to the entire North American continent and lie at the fringes of projected precipitation increases and decreases in most climate models (Trenberth, 2011). In California, for example, both the peak and the onset of the precipitation season have been delayed, yet these shifts have not significantly impacted overall precipitation levels (Luković et al., 2021). According to studies on the effect of sea surface temperature on IVT, ARs should have seen a notable enhancement post-1970 (Huang et al., 2020); however, such enhancement is not evident in current records. In fact, the increase in surface temperatures has been even more rapid, with winter LST already rising by more than 2 degrees Celsius since 1980 (Gonzales et al., 2019). These changes highlight the need to study the impact of land surface temperature on AR-induced precipitation patterns. Given that the overall change in total precipitation is not pronounced, the shift in the distribution of extreme precipitation under climate change must be attributed to factors other than merely an increase in water vapor (Neiman et al., 2008). In this study, I concentrated on analyzing temperature changes preceding AR-induced precipitation events.

Data processing

All data cleaning, calculations, merges, and visualizations were conducted using a Jupyter Notebook, programmed in Python 3. The bulk of the continuous meteorological data was stored in NetCDF format (Rew et al., 1989), while the SIO-R1 catalog was stored in text format. MERRA-2 data is organized daily, while SIO-R1 data is cataloged annually. The occurrence of leap years, as well as leap years with or without precipitation days, posed a challenge to data alignment. Despite efforts to minimize the impact on the synchronization of datasets, the data for December 31, 2012, remained elusive. The data was primarily read and linked to the information in the SIO-R1 catalog, correlating the contents of the NetCDF and text files, and assigning an ARID to each event for tracking purposes. In this process, it became evident for the first time that some AR events occurred without any associated precipitation. Subsequent data analysis was then performed on the IVT and precipitation data. Following this, MERRA-2 data was read and cross-referenced against the existing ARIDs. During this comparison, events lacking precipitation data were excluded, and temperature variables were incorporated. The maximum surface temperature preceding each event was then aligned with its corresponding ARID. Typically, this maximum

temperature occurred 6 hours before the precipitation event, although occasionally it was 3 hours. Once all resolutions and timings were matched and verified, data visualization and analysis were conducted anew.

Clausius-Clapeyron and hypothesis test

When discussing the effects of climate change on precipitation, the concept of saturated vapor pressure is indispensable. Unlike the uncertainties associated with changes in precipitation distribution and extreme precipitation events, the increase in water vapor associated with climate change is notably consistent. The Clausius-Clapeyron equation delineates how the capacity of air to carry water vapor (q) increases with temperature:

$$\frac{1}{\Delta T_s}\frac{\Delta q}{q} = \alpha(T)\frac{\Delta T}{\Delta T_s}$$

Where α(T) represents the scaling factor of the Clausius–Clapeyron equation and is defined as:

$$\alpha(T) = \frac{L}{R_v T^2}$$

For surface temperatures characteristic of ARs making landfall in California in the present climate, with an average LST of 13 °C, the scaling factor α(T) is approximately 6.6% per Kelvin (Dettinger, 2011). This basic thermodynamic response is one of many factors that affect IVT strength and AR intensity. The conversion ratio of IVT to precipitation is subject to even greater influence (Payne et al., 2020). The increases in water vapor resulting from rises in SST or LST are not anticipated to surpass 14%. Yet, such changes cannot be solely attributed to the Clausius-Clapeyron relationship when observing AR precipitation (Michaelis et al., 2022). This indicates that other factors also influence precipitation in ARs, including but not limited to topography, the vertical profile of the atmosphere, and temperature anomalies (Gimeno et al., 2014; Corringham et al., 2019; Huang et al., 2020). I conducted a hypothesis test on latitude to investigate its potential influence on the relationship between temperature and AR intensity. I segmented my research area into three latitudinal zones and performed data analysis independently for each region.

RESULTS

Seasonality and distribution

The temporal distribution and frequency of AR events from 1995 to 2015 show a seasonal pattern, with certain periods experiencing higher frequencies of events. This pattern is evident when examining the percentage of AR events occurring on each day throughout the 21-year period (Figure 2). The overlay of data points across each year reveals fluctuations in the daily occurrence of AR events, highlighting specific times when these events are more prevalent. A clear pattern emerges from the overlay of data points, indicating a degree of seasonality in the occurrence of AR events.

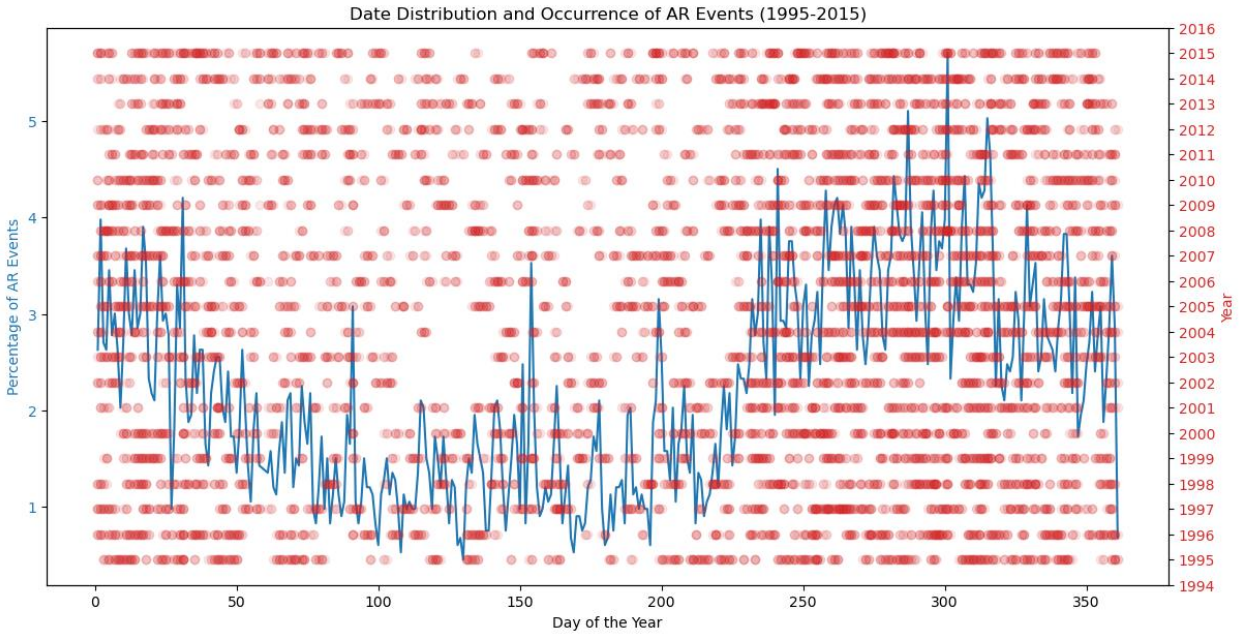

Figure 2. Date Distribution and Occurrence of AR Events from 1995-2015. This time series graph displays AR events per day over a 21-year period. Each year is represented by a distinct set of data points plotted along the horizontal axis, which corresponds to days of the year (colored red), while the vertical axis (colored blue) quantifies the percentage of AR events occurring on each day.

A clearer seasonal trend emerges with the analysis of the monthly distribution, with peaks in occurrence during certain months in the winter season. The variability within individual years around the overall monthly trend underscores the interannual differences in the occurrence of AR events. Each line representing a year adds to the complexity of the pattern, culminating in an

overlaid line that delineates the aggregated monthly percentage (Figure 3). The individual years demonstrate variability around the aggregate trend, indicating interannual differences in the monthly distribution of AR events. As evident from the graph, the year-to-year changes are very pronounced, with hardly any year perfectly conforming to the overall pattern. A less pronounced trend observed is the delay in the onset of the peak rainy season, shifting from September to October over the years.

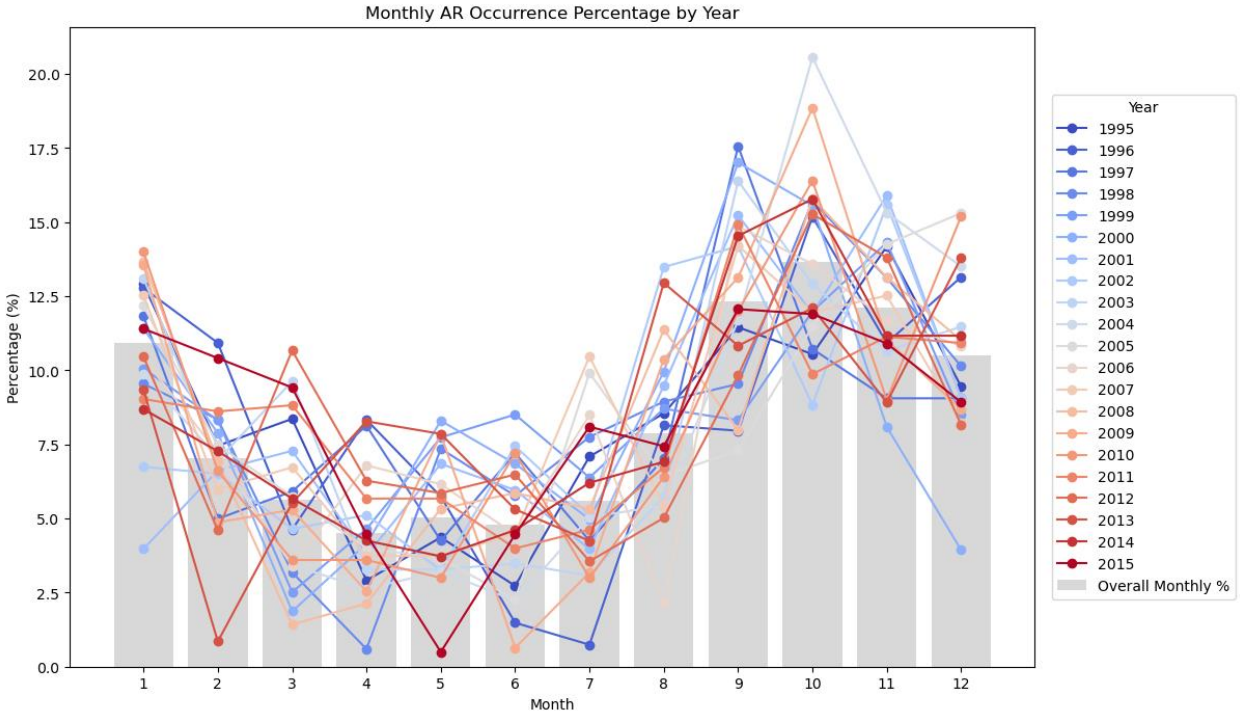

Figure 3. Monthly AR Occurrence Percentage by Year. This line graph illustrates the monthly distribution of AR events over the years. Each line corresponds to a different year, with the overall monthly percentage of AR events represented by an overlaid line marked with distinct symbols.

The mapping of significant AR-related precipitation events that exceed 100 mm/day demonstrates a concentrated spatial distribution along certain regions, particularly along coastal areas (Figure 4). Areas with the highest frequency and intensity of AR precipitation events are highlighted by clusters of warmer colors. The distribution pattern shows a concentration of significant AR events along specific geographic regions. This distribution pattern is strongly correlated with topographic variations, indicating three distinct concentration zones from the coast to the Rockies, corresponding to areas with significant topographical changes. The latitude

distribution appears relatively random, and I will maintain this assumption until conducting the hypothesis test.

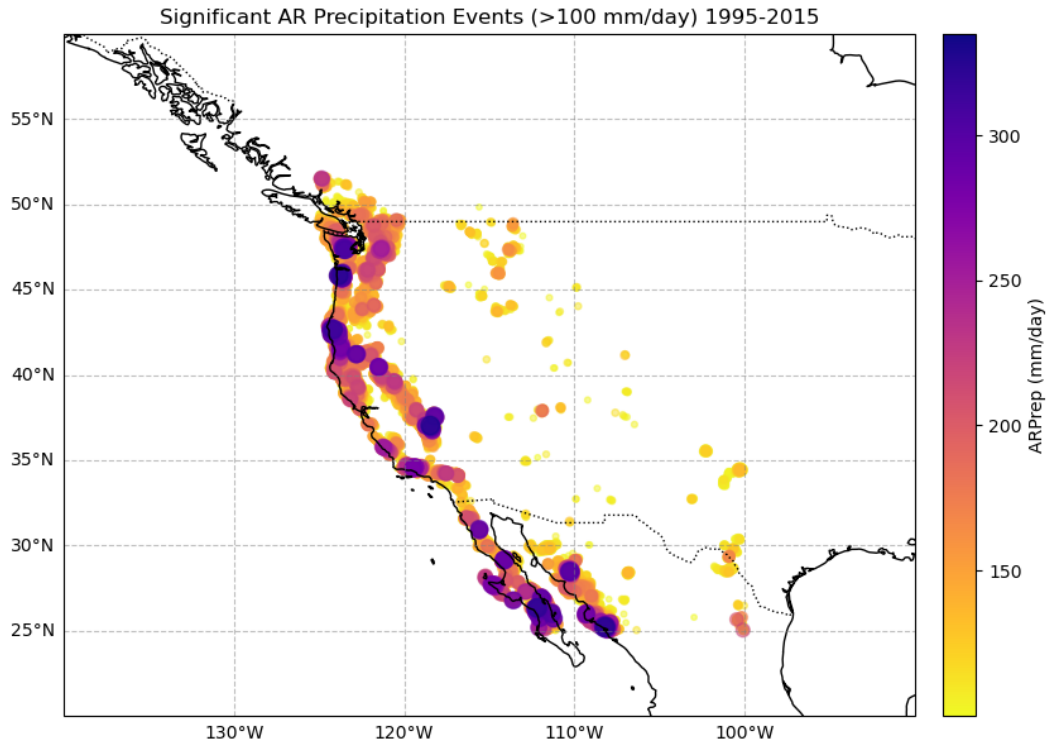

Figure 4. Significant AR Precipitation Events from 1995-2015. This geographic map highlights areas with significant AR-related precipitation events exceeding 100 mm/day. The intensity and frequency of these events are represented by the size and color of the dots, with warmer colors indicating higher frequencies.

Collectively, the data underscores the seasonality and spatial distribution of AR events over the two decades, highlighting areas with higher susceptibility to such events. The variability observed in both daily and monthly analyses, coupled with the geographic patterns of precipitation intensity, provides a foundational understanding of AR climatology. This allows me to utilize 20 years of data to discern the effects of climate change from seasonal distribution patterns.

IVT and precipitation

The conversion from water vapor to precipitation is inherently a nonlinear process, influenced by numerous factors. I analyzed IVT and precipitation to determine whether the observed conversion ratio differed under the peak and mean values of each event (Figure 5). I also

compared their averages to extremes (Figure 5c, 5d). Given that duration is another indicator of ARs, it is possible that the effects of longer precipitation events could still be significant, even at lower peak intensities.

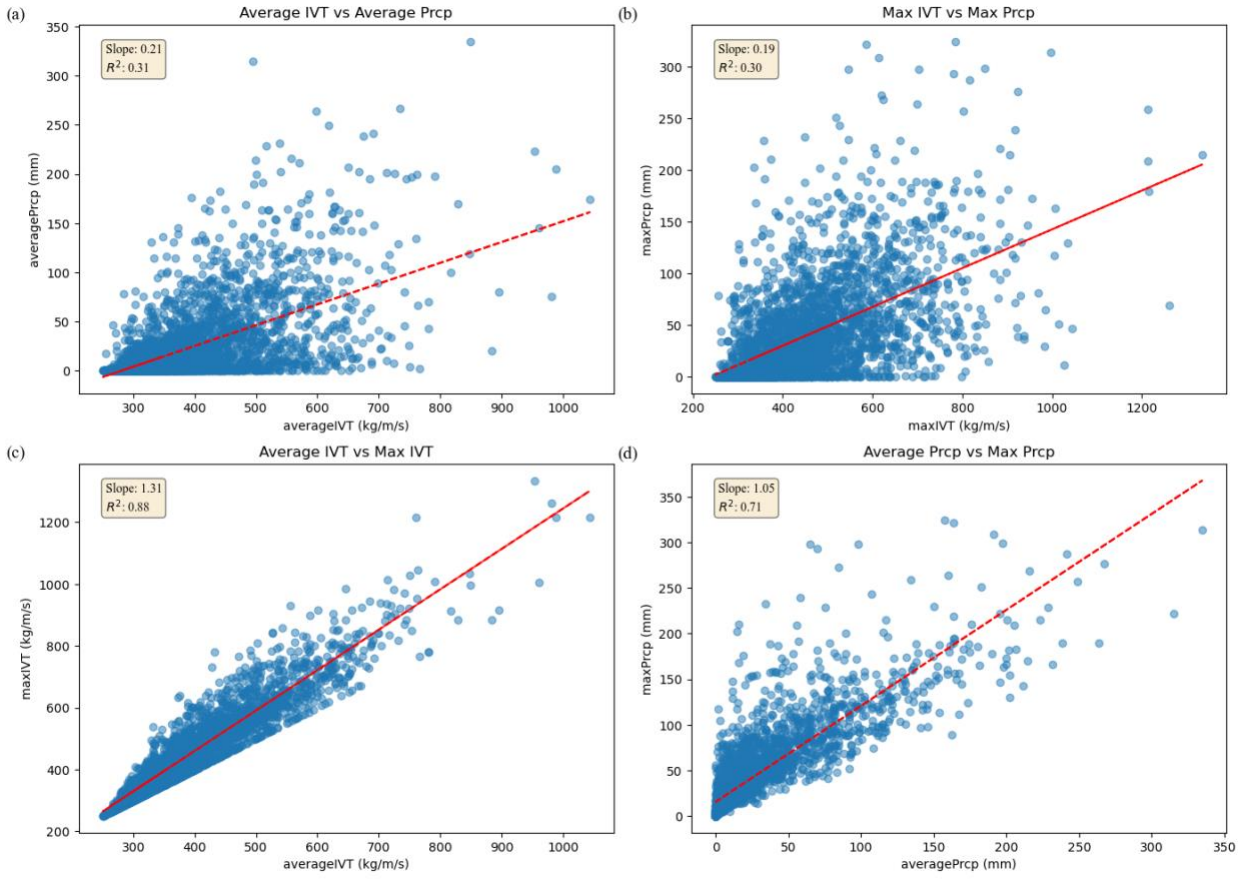

Figure 5. Integrated Vapor Transport vs. Precipitation Analysis. This set of scatter plots illustrates the relationship between IVT and precipitation intensity for each AR-induced precipitation event. Subplots include: (a) average IVT vs. average precipitation, (b) maximum IVT vs. maximum precipitation, (c) average IVT vs. maximum IVT, and (d) average precipitation vs. maximum precipitation. Trend lines are included to indicate general trends, though they are not statistically significant.

The relationship between IVT and precipitation is generally positive, although the R2 values for both the maximum and mean correlations are very low. Interestingly, the data shows a large number of high precipitation events occurring at lower IVT states (Figure 5a). This further underscores that the intensity of precipitation, particularly during occasional extreme events, cannot be directly predicted by IVT alone (Figure 5b). An internal comparison reveals that the ratio between maximum and average IVT is consistently greater than 1, indicating that peak IVT closely resembles the overall water vapor content (Figure 5c). However, the distribution of

precipitation is more dispersed, with many instances where higher average values correspond to lower maximum values (Figure 5d). Such inconsistencies between IVT and precipitation are largely attributable to other unconsidered factors and their physical properties.

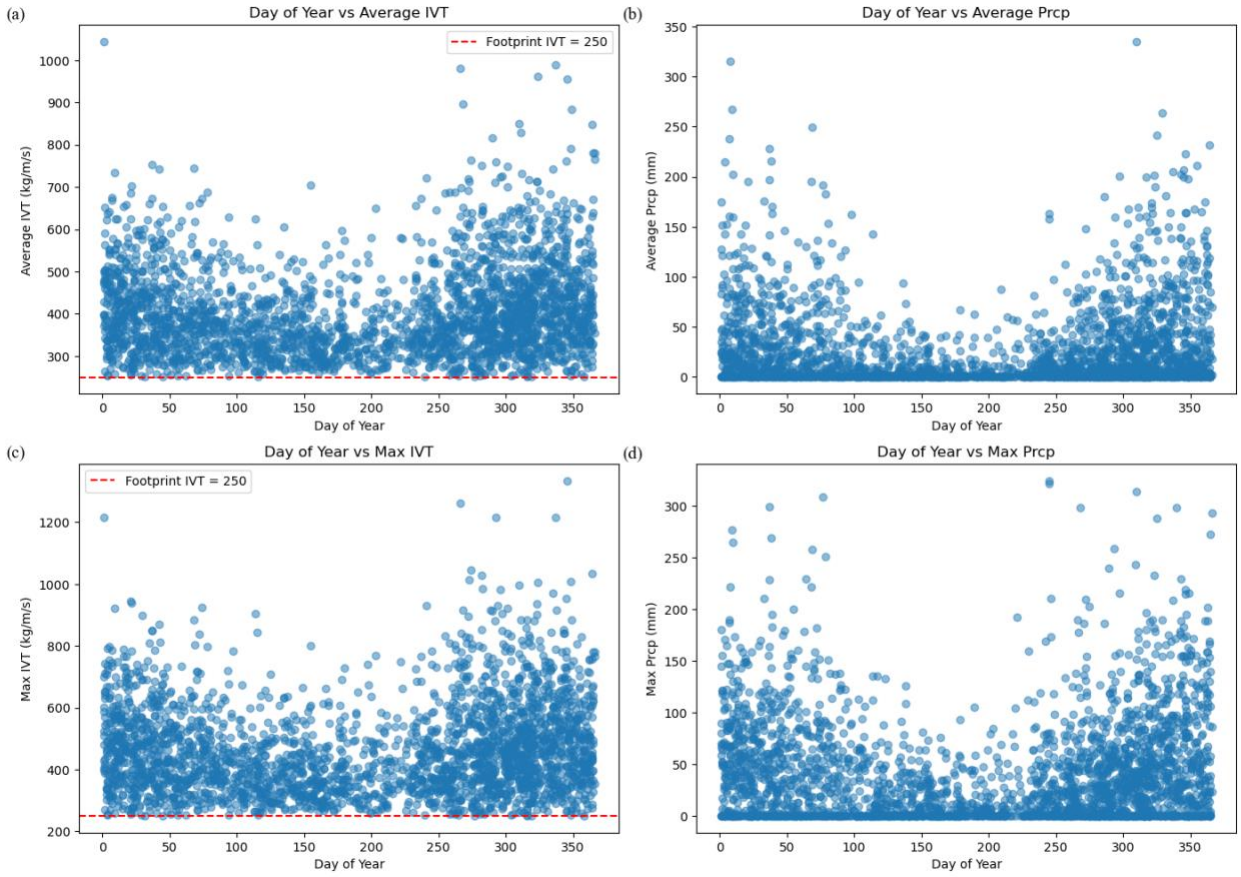

Figure 6. IVT and Precipitation Patterns, Day of Year. This composite graph displays the relationship between day of the year and AR characteristics, with subplots showing: (a) average IVT, (b) average precipitation, (c) maximum IVT, and (d) maximum precipitation. IVT values exceeding 250 kg/m/s are noted as indicative of an AR footprint.

The annual distribution of AR-induced precipitation events also provides additional insights (Figure 6). Because water has a higher specific heat capacity compared to land, the rate of change and magnitude of SST variations are smaller than those of LST. Previous studies have demonstrated the relationship between IVT and SST (Chen and Leung 2020). This association, coupled with the disparity between LST and SST, contributes to the reduced variability in the overall IVT values (Figure 6a, 6c). The persisting seasonality of IVT is linked to the fact that the SIO-R1 catalog I used records only landfalling ARs. The mean distribution of precipitation exhibits strong seasonality, whereas the distribution of maximum precipitation displays greater randomness (Figure 6b, 6d). With the increase in surface temperature during summer, even a

smaller content of water vapor can trigger short-term heavy rainfall events through convective processes within a brief period. This further reinforces the notion that Maximum IVT cannot directly represent AR-induced precipitation intensity.

LST and AR events

LST exhibits larger transient variability compared to precipitation and IVT. Initially, temperature anomaly was the preferred metric for exploring differences between temperature before rainfall and average temperature. However, due to challenges in extracting and identifying 3-hour high precision temperature anomaly data, I opted to select the highest temperature before rainfall. This temperature metric exhibits a wide distribution owing to variations within the 24-hour day and across different latitudes and altitudes in various seasons (Figure A1). By comparing1995 and 2015, we can observe the following trends (Figure 7).

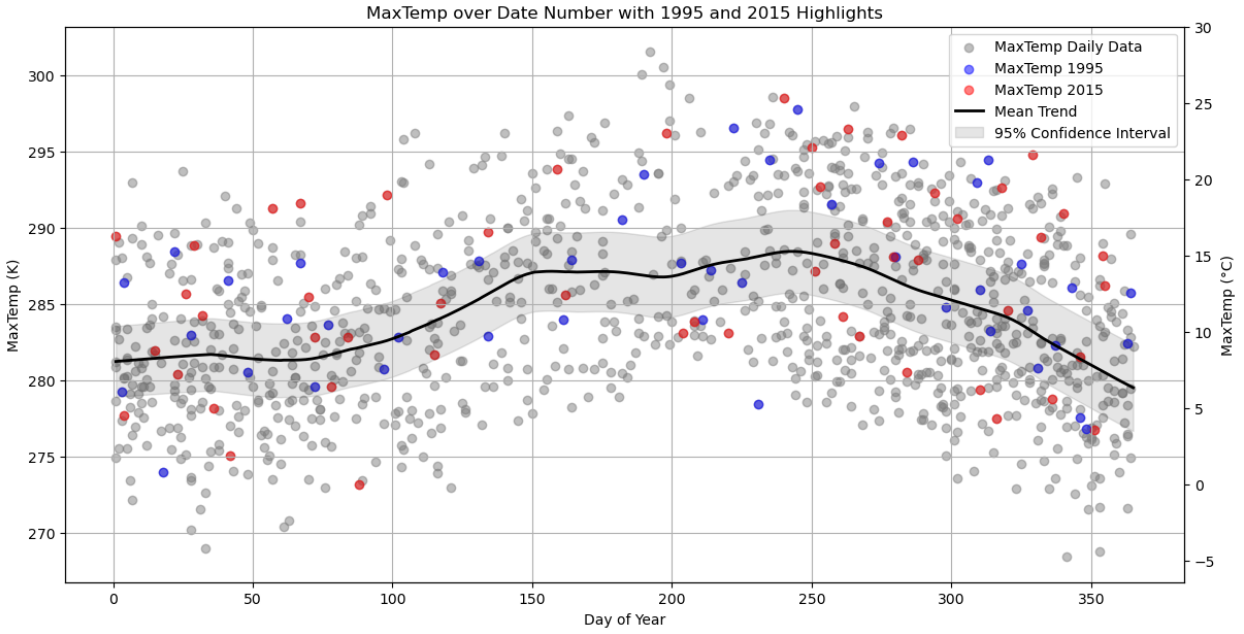

Figure 7. Maximum Pre-landfalling LST Distribution, with 1995 and 2015 Highlighted. This graph plots the maximum LST before AR landfall over the year, showcasing trends and variations. Data points from 1995 and 2015 are highlighted, with an average trend line and shaded confidence intervals to show distribution spread.

The distribution of LST exhibits a general seasonal pattern, albeit with strong variation. Additionally, upon comparing temperatures in 1995 and 2015, we note that the mean change is not substantial. However, there is a notable increase in the frequency of above-average temperatures

towards the end of 2015. Several factors could contribute to this effect, but it aligns with the monthly distribution data indicating a delayed onset of the rainy season. Based on the distribution, I conducted an analysis of the relationship between LST and AR (Figure 8).

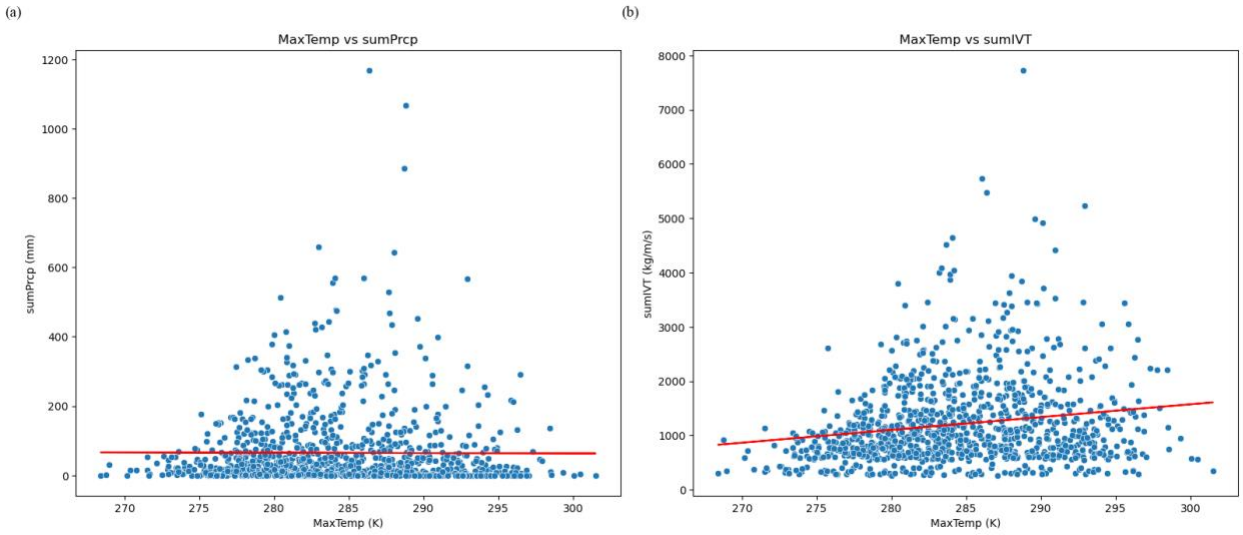

Figure 8. The Interrelationship between LST and AR. This scatter plot examines the correlation between pre-landfall LST and AR characteristics: (a) cumulative precipitation, and (b) cumulative IVT. The trend line serves as a visual guide without statistical significance, highlighting the general distribution of data points.

The distribution of points reveals a concentration of data with low precipitation values across the temperature spectrum (Figure 8a). However, as maximum temperatures increase, there is a slight uptick in precipitation totals, indicated by a small number of data points shifting upward. This relationship is weak, as the majority of data points remain clustered around the baseline. However, considering seasonal variations, even minor temperature changes during the precipitation season can lead to exponential increases in the likelihood of maximum precipitation.

In contrast, as maximum temperature rises, the sum of IVTs also increases (Figure 8b). Unlike precipitation, the distribution of points is more dispersed and exhibits a clear upward trend. This suggests that higher surface temperatures may be associated with increased water transport during AR events. There is a strong correlation between SST and LST in both diurnal and seasonal trends, which might explain the relationship we observed. However, it still indicates a trend of maximum precipitation increasing with rising LST, suggesting a potential exponential increase. When comparing the distribution of IVT and precipitation, it can be observed that the highest peak of precipitation occurs at around 285K, whereas the highest peak of IVT occurs at 290K. Beyond 290K, precipitation decreases rapidly to near the average level, while IVT maintains high. These

temperatures mainly occur in summer, which aligns with the observation that there is minimal precipitation during summer despite the persistence of a higher IVT.

Latitude influence on IVT, precipitation, and LST relationship

The relationship between IVT, precipitation, and LST across different latitudes provides insight into the geographical variability of AR events. This section focuses on the data for the latitude band 45-55 degrees (Figure 9 and Figure 10), with additional latitude bands 25-35 degrees and band 35-45 degrees in Appendix B (Figure B1-B4). These analyses employed the same methods as the previous ones (Figure 5, Figure 8) and were divided by different latitudes to assess the impact of latitude on the observed results. The analysis reveals that the variation in IVT versus precipitation was not significant, and there were no discernible latitude characteristics in precipitation (Figure 9, Figure B1, Figure B2). No significant difference can be seen in IVT and precipitation intensity. Specific images can be found in Appendix B (Figure B5, Figure B6). Seasonal trends are directly related to latitude (Figure 11).

Latitude emerged as a crucial factor in the influence of LST. At high latitudes, both precipitation intensity and IVT increased with the rise of LST (Figure 10). Conversely, this trend was reversed at lower latitudes (Figure B3). This highlights the importance of considering latitude and climate zone influences on temperature changes when examining the impact of climate change on AR-induced precipitation. It also underscores the concept of a climate change threshold, prompting the consideration of whether temperature changes have altered seasonal behavior rather than solely affecting water vapor and precipitation conversion rates.

The seasonal characteristics are particularly pronounced in different latitudinal regions. Apart from the variation in mean values, there are also distinct peak events associated with ARs. Notably, for the middle and high latitudes, the onset of the rainy season occurs significantly earlier compared to the lower latitudes (Figure 11). Regarding precipitation types, except for areas below 0 degrees latitude where precipitation occurs at lower temperatures, the majority of AR-induced precipitation still falls in the form of rain. These lower-temperature precipitation events and their respective forms are highly sensitive to temperature increases, leading to significant changes in local hydrological characteristics.

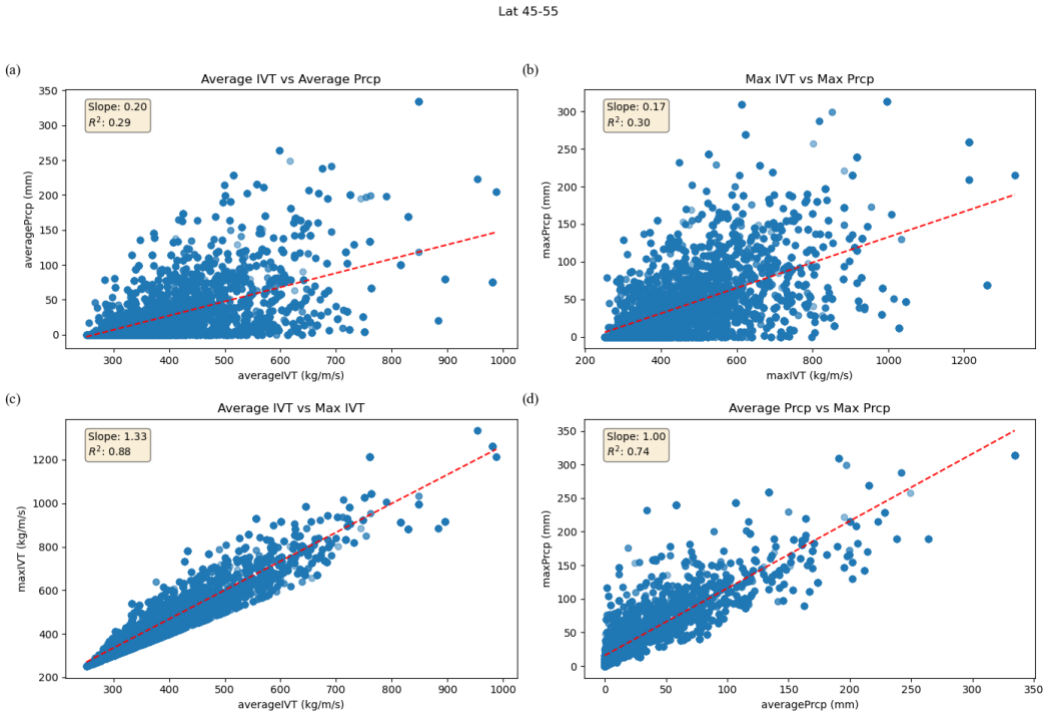

Figure 9. IVT vs. Precipitation Analysis in latitude range 45°N-55°N. This series of scatter plots displays the relationship between integrated water vapor transport (IVT) and precipitation intensity at this specific latitude range. The subplots include: (a) average IVT vs. average precipitation, (b) maximum IVT vs. maximum precipitation, (c) average IVT vs. maximum IVT, and (d) average precipitation vs. maximum precipitation.

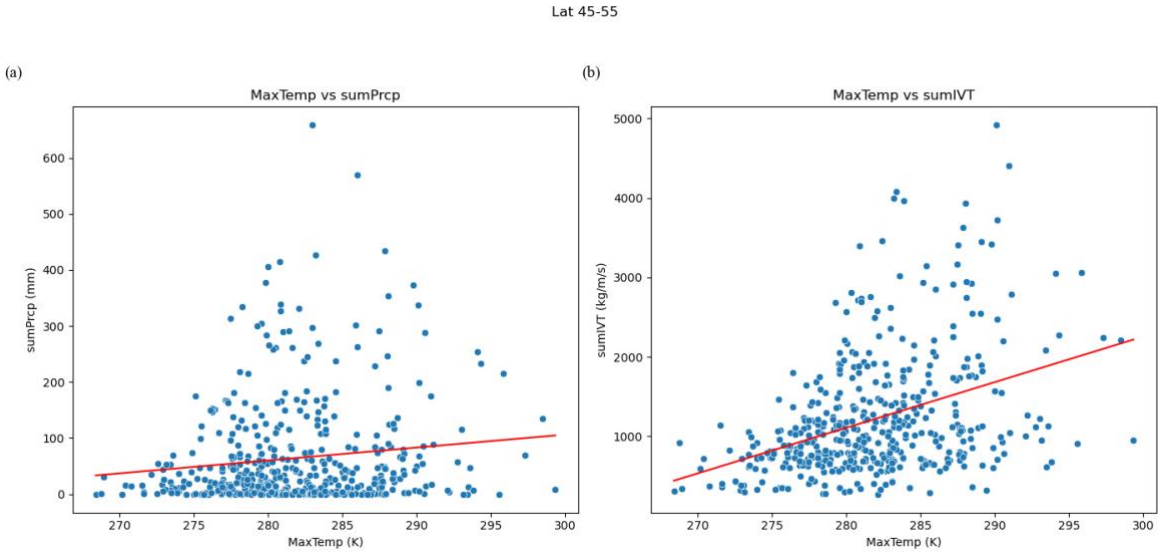

Figure 10. The Interrelationship between LST and AR in latitude range 45°N-55°N. This scatter plot explores the correlation between land surface temperature (LST) prior to AR landfall and AR characteristics such as cumulative precipitation and IVT in this latitude range. The graph provides a visual guide to the distribution trends without statistical significance.

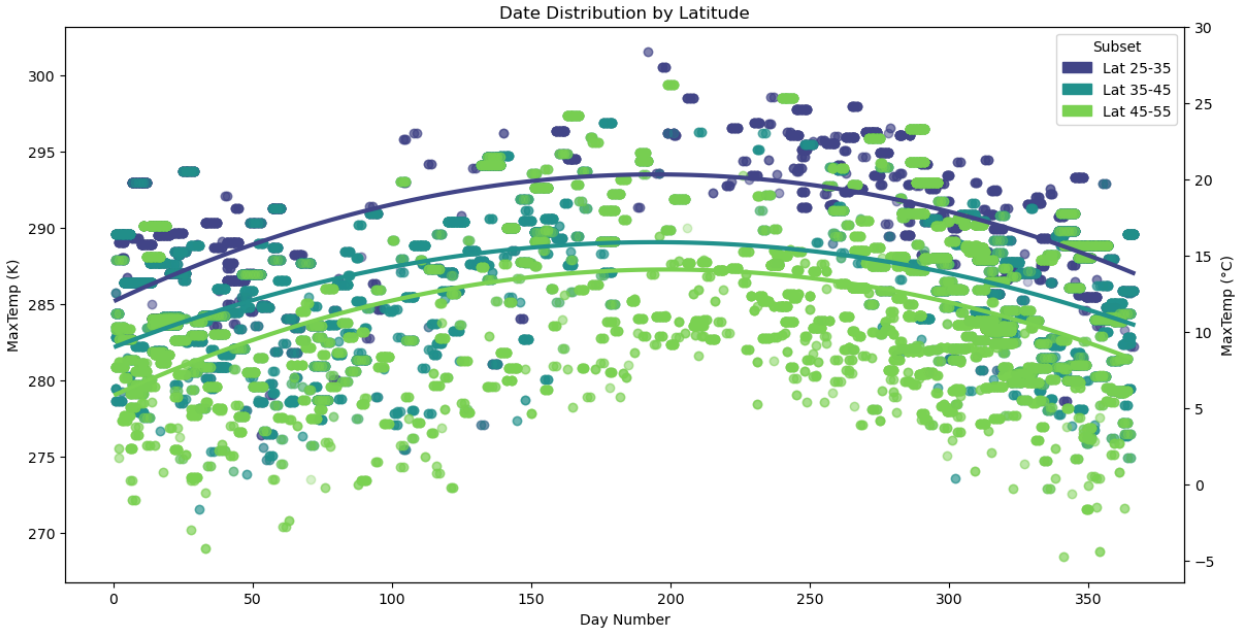

Figure 11. Maximum Pre-landfalling LST Distribution under Latitude Control. This graph presents the maximum LST before AR landfall across different latitude zones, plotted against the day of the year. Color coding differentiates the latitude zones, highlighting seasonal trends in LST variations.

While my study did not analyze the paths and durations of ARs, it is known that the paths of ARs are primarily influenced by circulation and subtropical high guidance (Cordeira et al., 2013). Additionally, the duration of AR is strongly correlated with water vapor supply, and longer durations tend to correspond to higher peak IVT values (Zhou et al., 2018). Although this correlation was not directly examined in my study, the high correlation between mean IVT and maximum IVT suggests a similar concept (Figure 5c). These changes become more pronounced with increasing latitude, particularly in the middle and high latitudes (Figure 10b).

DISCUSSION

In this thesis, I explored the influence of land surface temperatures (LST) on atmospheric river (AR)-induced precipitation along the west coast of North America from 1995 to 2015, utilizing the SIO-R1 catalog and MERRA-2 model. My analysis revealed pronounced seasonality in AR events and a correlation with fluctuations in LST, providing insights into the efficiency of water vapor conversion to precipitation under varying conditions (Figures 2, 3, 4, 5, 6). I addressed a significant gap in understanding AR dynamics in the context of climate change, demonstrating that higher pre-precipitation LSTs are linked to increased likelihood and intensity of extreme precipitation events, especially at higher latitudes (Figure 10). This finding suggests that local temperature anomalies could serve as predictive tools for assessing AR impacts, supported by the observed interplay between LST and AR dynamics across various latitudes (Figures 9 and 10; Appendix B). Furthermore, I delved into the causative mechanisms behind these correlations, examining how global warming might be redefining hydrological dynamics on North America's west coast (Michaelis et al. 2022). By mapping these patterns against broader climatic shifts (Figure 11), I contributed to the discourse on climate resilience and adaptive strategies, which are crucial for managing risks associated with extreme weather events driven by atmospheric rivers, as evidenced by the significant variability in AR behavior (Gershunov et al. 2017; Dettinger 2011).

Seasonality and delay rainy season

The delayed onset of the rainy season, as evidenced by the timing of AR events, reflected a deviation from historical weather patterns (Figure 2, Figure 3). I noted this delay in the interannual variability of AR frequency, which could indicate a shift in climatic conditions, potentially associated with increased global temperatures (IPCC 2023). I observed the same delay in observational data, with a smaller geographical feature making the tendency to delay even more pronounced (Luković et al. 2021). Such changes necessitated a reassessment of water resource strategies to accommodate later start times for seasonal precipitation. My observations aligned with projections suggesting a redefinition of seasonality due to climate change, where the temporal dynamics of ARs and their associated precipitation are subject to shifts (Swain et al. 2018). A

broader understanding of these shifts offered valuable insights into the long-term planning required to adapt to changing precipitation patterns.

Considering that the path of ARs is related to fluctuations in jet streams, changes in jet streams under climate change also influenced their paths (Woollings et al. 2023). The relationship between local temperature and short-duration rainfall was greater than the 6-7% moisture growth, consistent with my data (Schroeer and Kirchengast 2018). Currently, the temperature change in my data was not obvious (Figure 7), but in other meteorological data models with a larger scope, winter temperatures had increased significantly (Gonzales et al. 2019; Trenberth and Shea 2005). Seasonality and the delay in the rainy season were critical considerations for future climate modeling and social adaptation efforts.

Clausius-Clapeyron relationship and inconsistency

The Clausius-Clapeyron relationship did not fully capture the observed escalation of precipitation intensity from ARs in a warming climate (Figure 5). The complexities of atmospheric responses to LST changes seemed to amplify precipitation beyond the expected theoretical increase in water vapor capacity (Dettinger 2011; Payne et al. 2020). These findings pointed towards the need for an enhanced modeling framework that could account for additional atmospheric processes and feedbacks that might intensify the water vapor-precipitation relationship in AR scenarios (Michaelis et al. 2022). Contemporary numerical models consistently projected a notable increase in extreme precipitation, with estimates surpassing 7%/K in both frequency and intensity. However, given the limited availability of water vapor supply, an increase in extreme AR events inevitably resulted in a shift in the overall AR trend (Payne et al. 2020). This adjustment required compromises in one or more dimensions such as frequency, duration, and spatial distribution to accommodate the heightened extremes in precipitation intensity.

Vertical profile, topology, and convection

The vertical atmospheric profile and land topology appeared to modulate the impact of LST on AR precipitation efficiency (Figure 8). Complex interactions between the rising LST and the atmosphere's vertical structure led to an increased conversion of water vapor to precipitation.

Additionally, convection processes, intensified by higher pre-AR event temperatures, contributed to the variability and intensity of precipitation, especially in topographically diverse regions such as the North America West Coast. Topography and LST could alter precipitation form as well as intensity. Higher surface and vertical profile temperatures allowed more precipitation to fall as rain rather than snow. This effect significantly increased flood and drought risks (Corringham et al. 2019). The phenomenon of surface temperature changes influencing precipitation patterns was initially observed and modeled in the Amazon rainforest (Swann et al. 2015). With the amplification of the urban heat island effect under climate change, convectively available potential energy (CAPE) at the urban scale was anticipated to undergo alterations in the future. This shift was poised to contribute to an uptick in extreme rainfall events at the local level, carrying more pronounced social ramifications than changes in the mean. Additionally, the projected increase in total precipitation coupled with a decrease in snowfall was forecasted to result in a significant surge in peak runoff alongside a notable decline in dry season runoff (Huang et al. 2020). Such dynamics could exacerbate California's water crisis and escalate wildfire risks, introducing heightened secondary hazards alongside direct heavy rainfall events (Landauer et al. 2019).

Latitude and general pattern

The impact of LST on AR dynamics exhibited a pronounced latitudinal variation (Figures 9 and 10). At higher latitudes, increased LST correlated with a significant rise in both precipitation intensity and IVT, whereas at lower latitudes, these relationships were less evident (Figure B3). When considering latitude blocks, selecting the corresponding region was crucial. Numerous studies have focused on specific regions such as California (Ryoo et al. 2015; Corringham et al. 2019; Luković et al. 2021; Michaelis et al. 2022). However, Oregon, also situated on the west coast of North America, has substantially less available data compared to Washington and California, which are located further north. Climate models commonly partition regions based on climate categories (Iturbide et al. 2020), but for AR models, the presence of a diverse mix of topographical features can yield varied results. Understanding these regional variations was essential for accurately assessing the impacts of ARs across different geographical areas. ARs wield significant influence globally, with their substantial water vapor transport serving as a pivotal factor in shaping future rainfall patterns (Paltan et al. 2017). The impact of latitude determined whether these

changes manifested positively or negatively. This latitude dependency underscored the crucial role of regional climatic factors in shaping the intricate interplay between temperature and precipitation during AR events. Consequently, a targeted approach in climate impact studies was essential to comprehensively understand and address the implications of AR dynamics across different geographical regions. While ARs carry substantial water vapor, their lower energy and shorter duration render them less concerning outside of directly affected areas. This has, in turn, contributed to a partial delay in the study of more detailed physical mechanisms. Studying the physical dynamics in more detail was crucial for further modeling of AR.

Limitations

The temporal scope of this study, limited to a 21-year period, was a primary constraint, stemming from the need to balance the extensiveness of data with the focus of the research topic. While this duration permitted an examination of seasonal patterns and their deviations, it might not have captured the full spectrum of climate change impacts over more extended periods (Figure 2). Consequently, this limitation directed the exclusion of climate projections from the analysis. The dataset may not have sufficiently revealed the intricate relationships between climate variables that are essential for understanding the long-term trends of climate change. The temperature data, measured three hours prior to rainfall events, could potentially mask the subtle temperature anomalies pivotal to changes in rainfall conversion rates. The use of a 24-hour average temperature might have inadvertently integrated the cooling effect of precipitation itself, skewing the analysis of LST's influence on precipitation (Figure 7). Addressing these concerns would require access to higher-resolution AR datasets and refined algorithms capable of discerning between pre-precipitation temperature anomalies and the cooling effects of rainfall.

The lower resolution of the AR data, coupled with discrepancies between different climatological systems, further compounded the study's limitations (Figure 9). Such inconsistencies could obscure the nuances of AR behaviors and the resultant precipitation patterns, particularly when correlating IVT and LST with precipitation outputs. A future expansion of this study might involve integrating higher-resolution data and standardizing across meteorological systems to improve consistency and reliability in the findings. Subsequent hypothesis testing, especially in relation to temperature anomalies and their role in precipitation efficiency, will

require these improvements to yield more definitive insights into the mechanisms driving AR-related weather events.

Future direction and Broader implications

Advancing the understanding of atmospheric rivers and their interactions with land surface temperatures and sea surface temperatures will be crucial for enhancing predictive models and developing more effective mitigation strategies (Gelaro et al., 2017). Researchers should incorporate a more detailed examination of the vertical profiles of atmospheric rivers to understand the dynamics of moisture transport and precipitation processes more precisely. Convection in tropical regions exhibits an aggregation state; however, it remains unclear whether this state occurs in mid-latitudes, particularly in AR-induced precipitation (Angulo-Umana and Kim, 2023). Expanding the scope of hypothesis testing clarified the relationships between atmospheric variables, leading to more direct and actionable insights. Additionally, variance analysis helped clarify the consistency of relationships across different models, aiding in the refinement of climate projections (Chen and Leung, 2020). On a practical level, improvements in atmospheric river reporting systems significantly enhanced the timeliness and accuracy of weather forecasts, vital for emergency preparedness (Figure C1). Strengthening public awareness and planning for more intense precipitation events, especially in regions frequently affected by atmospheric rivers, was also essential (Michaelis et al., 2022). This approach not only aligned with the need for more comprehensive climate adaptation strategies but also ensured that communities were better prepared to handle the impacts of extreme weather events. By extending these efforts, researchers fostered greater resilience against the backdrop of evolving global climate conditions (Figures 9 and 10). In conclusion, my thesis provided actionable insights that can be leveraged to enhance climate resilience, empowering policymakers and planners to better safeguard vulnerable communities and ensure a more sustainable future in the face of evolving global climate conditions.

ACKNOWLEDGEMENTS

I am deeply grateful to everyone who made it possible for me to complete this thesis. I particularly thank my mentor, Professor John Chiang from the Department of Geography, for his invaluable suggestions and encouragement, which were crucial in coordinating and writing this thesis. I would also like to thank Annie Miller for her thoughtful feedback and patient guidance during office hours, providing me with affirmation and support when my progress lagged behind others. I want to acknowledge the support of Patina Mendez, Matthew Bodo, and all the ES staff whose efforts made my one-and-a-half-year journey possible. My data support came from Dr. Sol Kim, who provided me with a usable catalog and taught me how to interpret the data at the beginning of my research, saving me time to focus on more valuable parts of my work. Thanks to UC San Diego's Scripps Institute of Oceanography, WECLIMA's open-source database, and NASA's MERRA-2 open-source model for supporting my research. Special thanks go to Professor Cort Anastasio from UC Davis; Professors Inez Fung and Dennis Baldocchi from the Department of ESPM/EPS, Josh Apte and Mark Stacey from the Department of Civil Engineering, and Dr. Michael Alves from UC Berkeley, who guided me and provided support during my studies on climate change and the conduct of this thesis. Thanks to the College of Natural Resources, the Department of ESPM, and UC Berkeley for supporting my undergraduate degree with honor. Finally, I must express my gratitude to my ES peers—Mina Burns, Benjamin Weinberger, Claire Liu, Mara St. Amant, Patrick Jacobson, Xiangrong Sun, Priya Riley, and Bea Cundiff—who provided peer reviews, comments, and listened to my complaints when I was stuck on my research. I am thankful to my parents, who fully supported my pursuit of academics, and to all my friends who endured my frequent updates and musings over the past year and a half. I could not have completed this research and thesis without the help of everyone involved. Thank you again for all of your companionship over the past one and a half years!

REFERENCES

Angulo-Umana, P., and D. Kim. 2023. Mesoscale convective clustering enhances tropical precipitation. Science Advances 9:eabo5317.

Berg, P., J. O. Haerter, P. Thejll, C. Piani, S. Hagemann, and J. H. Christensen. 2009. Seasonal characteristics of the relationship between daily precipitation intensity and surface temperature. Journal of Geophysical Research: Atmospheres 114.

Change (IPCC), I. P. on C. 2023. Future Global Climate: Scenario-based Projections and Near-term Information. Pages 553–672 Climate Change 2021 – The Physical Science Basis: Working Group I Contribution to the Sixth Assessment Report of the Intergovernmental Panel on Climate Change. Cambridge University Press.

Chen, X., and L. R. Leung. 2020. Response of Landfalling Atmospheric Rivers on the U.S. West Coast to Local Sea Surface Temperature Perturbations. Geophysical Research Letters 47:e2020GL089254.

Cordeira, J. M., F. M. Ralph, and B. J. Moore. 2013. The Development and Evolution of Two Atmospheric Rivers in Proximity to Western North Pacific Tropical Cyclones in October 2010. Monthly Weather Review 141:4234–4255.

Corringham, T. W., F. M. Ralph, A. Gershunov, D. R. Cayan, and C. A. Talbot. 2019. Atmospheric rivers drive flood damages in the western United States. Science Advances 5:eaax4631.

DeRepentigny, P., A. Jahn, M. M. Holland, J. E. Kay, J. Fasullo, J.-F. Lamarque, S. Tilmes, C. Hannay, M. J. Mills, D. A. Bailey, and A. P. Barrett. 2022. Enhanced simulated early 21st century Arctic sea ice loss due to CMIP6 biomass burning emissions. Science Advances 8:eabo2405.

Dettinger, M. 2011. Climate Change, Atmospheric Rivers, and Floods in California – A Multimodel Analysis of Storm Frequency and Magnitude Changes1. JAWRA Journal of the American Water Resources Association 47:514–523.

Eiras-Barca, J., S. Brands, and G. Miguez-Macho. 2016. Seasonal variations in North Atlantic atmospheric river activity and associations with anomalous precipitation over the Iberian Atlantic Margin. Journal of Geophysical Research: Atmospheres 121:931–948.

Eyring, V., S. Bony, G. A. Meehl, C. A. Senior, B. Stevens, R. J. Stouffer, and K. E. Taylor. 2016. Overview of the Coupled Model Intercomparison Project Phase 6 (CMIP6) experimental design and organization. Geoscientific Model Development 9:1937–1958.

Gelaro, R., W. McCarty, M. J. Suárez, R. Todling, A. Molod, L. Takacs, C. A. Randles, A. Darmenov, M. G. Bosilovich, R. Reichle, K. Wargan, L. Coy, R. Cullather, C. Draper, S. Akella, V. Buchard, A. Conaty, A. M. da Silva, W. Gu, G.-K. Kim, R. Koster, R. Lucchesi, D. Merkova, J. E. Nielsen, G. Partyka, S. Pawson, W. Putman, M. Rienecker, S. D.

Schubert, M. Sienkiewicz, and B. Zhao. 2017. The Modern-Era Retrospective Analysis for Research and Applications, Version 2 (MERRA-2). Journal of Climate 30:5419–5454.

Gershunov, A., T. Shulgina, F. M. Ralph, D. A. Lavers, and J. J. Rutz. 2017. Assessing the climate-scale variability of atmospheric rivers affecting western North America. Geophysical Research Letters 44:7900–7908.

Gimeno, L., R. Nieto, M. Vázquez, and D. Lavers. 2014. Atmospheric rivers: a mini-review. Frontiers in Earth Science 2.

Gonzales, K. R., D. L. Swain, K. M. Nardi, E. A. Barnes, and N. S. Diffenbaugh. 2019. Recent Warming of Landfalling Atmospheric Rivers Along the West Coast of the United States. Journal of Geophysical Research: Atmospheres 124:6810–6826.

Gonzales, K. R., D. L. Swain, H. A. Roop, and N. S. Diffenbaugh. 2022. Quantifying the Relationship Between Atmospheric River Origin Conditions and Landfall Temperature. Journal of Geophysical Research: Atmospheres 127:e2022JD037284.

Hansen, J., M. Sato, P. Kharecha, and K. von Schuckmann. 2011. Earth's energy imbalance and implications. Atmospheric Chemistry and Physics 11:13421–13449.

Huang, X., D. L. Swain, and A. D. Hall. 2020. Future precipitation increase from very high resolution ensemble downscaling of extreme atmospheric river storms in California. Science Advances 6:eaba1323.

Iturbide, M., J. M. Gutiérrez, L. M. Alves, J. Bedia, R. Cerezo-Mota, E. Cimadevilla, A. S. Cofiño, A. Di Luca, S. H. Faria, I. V. Gorodetskaya, M. Hauser, S. Herrera, K. Hennessy, H. T. Hewitt, R. G. Jones, S. Krakovska, R. Manzanas, D. Martínez-Castro, G. T. Narisma, I. S. Nurhati, I. Pinto, S. I. Seneviratne, B. van den Hurk, and C. S. Vera. 2020. An update of IPCC climate reference regions for subcontinental analysis of climate model data: definition and aggregated datasets. Earth System Science Data 12:2959–2970.

Landauer, M., S. Juhola, and J. Klein. 2019. The role of scale in integrating climate change adaptation and mitigation in cities. Journal of Environmental Planning and Management 62:741–765.

Lavers, D. A., and G. Villarini. 2013. The nexus between atmospheric rivers and extreme precipitation across Europe. Geophysical Research Letters 40:3259–3264.

Luković, J., J. C. H. Chiang, D. Blagojević, and A. Sekulić. 2021. A Later Onset of the Rainy Season in California. Geophysical Research Letters 48:e2020GL090350.

Michaelis, A. C., A. Gershunov, A. Weyant, M. A. Fish, T. Shulgina, and F. M. Ralph. 2022. Atmospheric River Precipitation Enhanced by Climate Change: A Case Study of the Storm That Contributed to California's Oroville Dam Crisis. Earth's Future 10:e2021EF002537.

Mundhenk, B. D., E. A. Barnes, and E. D. Maloney. 2016. All-Season Climatology and Variability of Atmospheric River Frequencies over the North Pacific. Journal of Climate 29:4885–4903.

Neiman, P. J., F. M. Ralph, G. A. Wick, J. D. Lundquist, and M. D. Dettinger. 2008. Meteorological Characteristics and Overland Precipitation Impacts of Atmospheric Rivers Affecting the West Coast of North America Based on Eight Years of SSM/I Satellite Observations. Journal of Hydrometeorology 9:22–47.

O'Gorman, P. A. 2015. Precipitation Extremes Under Climate Change. Current Climate Change Reports 1:49–59.

Paltan, H., D. Waliser, W. Lim, B. Guan, D. Yamazaki, R. Pant, and S. Dadson. 2017. Global floods and water availability driven by atmospheric rivers. Geophysical Research Letters 44.

Payne, A. E., M.-E. Demory, L. R. Leung, A. M. Ramos, C. A. Shields, J. J. Rutz, N. Siler, G. Villarini, A. Hall, and F. M. Ralph. 2020. Responses and impacts of atmospheric rivers to climate change. Nature Reviews Earth & Environment 1:143–157.

Ralph, F. M., J. J. Rutz, J. M. Cordeira, M. Dettinger, M. Anderson, D. Reynolds, L. J. Schick, and C. Smallcomb. 2019. A Scale to Characterize the Strength and Impacts of Atmospheric Rivers. Bulletin of the American Meteorological Society 100:269–289.

Rew, R., G. Davis, S. Emmerson, C. Cormack, J. Caron, R. Pincus, E. Hartnett, D. Heimbigner, L. Appel, and W. Fisher. 1989. Unidata NetCDF. UCAR/NCAR - Unidata.

Ryoo, J.-M., D. E. Waliser, D. W. Waugh, S. Wong, E. J. Fetzer, and I. Fung. 2015. Classification of atmospheric river events on the U.S. West Coast using a trajectory model. Journal of Geophysical Research: Atmospheres 120:3007–3028.

Samset, B. H., C. W. Stjern, M. T. Lund, C. W. Mohr, M. Sand, and A. S. Daloz. 2019. How Daily Temperature and Precipitation Distributions Evolve With Global Surface Temperature. Earth's Future 7:1323–1336.

Schroeer, K., and G. Kirchengast. 2018. Sensitivity of extreme precipitation to temperature: the variability of scaling factors from a regional to local perspective. Climate Dynamics 50:3981–3994.

Shields, C. A., A. E. Payne, E. J. Shearer, M. F. Wehner, T. A. O'Brien, J. J. Rutz, L. R. Leung, F. M. Ralph, A. B. Marquardt Collow, P. A. Ullrich, Q. Dong, A. Gershunov, H. Griffith, B. Guan, J. M. Lora, M. Lu, E. McClenny, K. M. Nardi, M. Pan, Y. Qian, A. M. Ramos, T. Shulgina, M. Viale, C. Sarangi, R. Tomé, and C. Zarzycki. 2023. Future Atmospheric Rivers and Impacts on Precipitation: Overview of the ARTMIP Tier 2 High-Resolution Global Warming Experiment. Geophysical Research Letters 50:e2022GL102091.

Swain, D. L., B. Langenbrunner, J. D. Neelin, and A. Hall. 2018. Increasing precipitation volatility in twenty-first-century California. Nature Climate Change 8:427–433.

Swann, A. L. S., M. Longo, R. G. Knox, E. Lee, and P. R. Moorcroft. 2015. Future deforestation in the Amazon and consequences for South American climate. Agricultural and Forest Meteorology 214–215:12–24.

Trenberth, K. E. 2011. Changes in precipitation with climate change. Climate Research 47:123–138.

Trenberth, K. E., and D. J. Shea. 2005. Relationships between precipitation and surface temperature. Geophysical Research Letters 32.

Waliser, D. E., and J. M. Cordeira. 2020. Atmospheric River Modeling: Forecasts, Climate Simulations, and Climate Projections. Pages 179–199 in F. M. Ralph, M. D. Dettinger, J. J. Rutz, and D. E. Waliser, editors. Atmospheric Rivers. Springer International Publishing, Cham.

Woollings, T., M. Drouard, C. H. O'Reilly, D. M. H. Sexton, and C. McSweeney. 2023. Trends in the atmospheric jet streams are emerging in observations and could be linked to tropical warming. Communications Earth & Environment 4:1–8.

Xie, S.-P., C. Deser, G. A. Vecchi, J. Ma, H. Teng, and A. T. Wittenberg. 2010. Global Warming Pattern Formation: Sea Surface Temperature and Rainfall. Journal of Climate 23:966–986.

Zhou, Y., H. Kim, and B. Guan. 2018. Life Cycle of Atmospheric Rivers: Identification and Climatological Characteristics. Journal of Geophysical Research: Atmospheres 123:12,715-12,725.

APPENDIX A: Pre-landfall Temperature Distribution

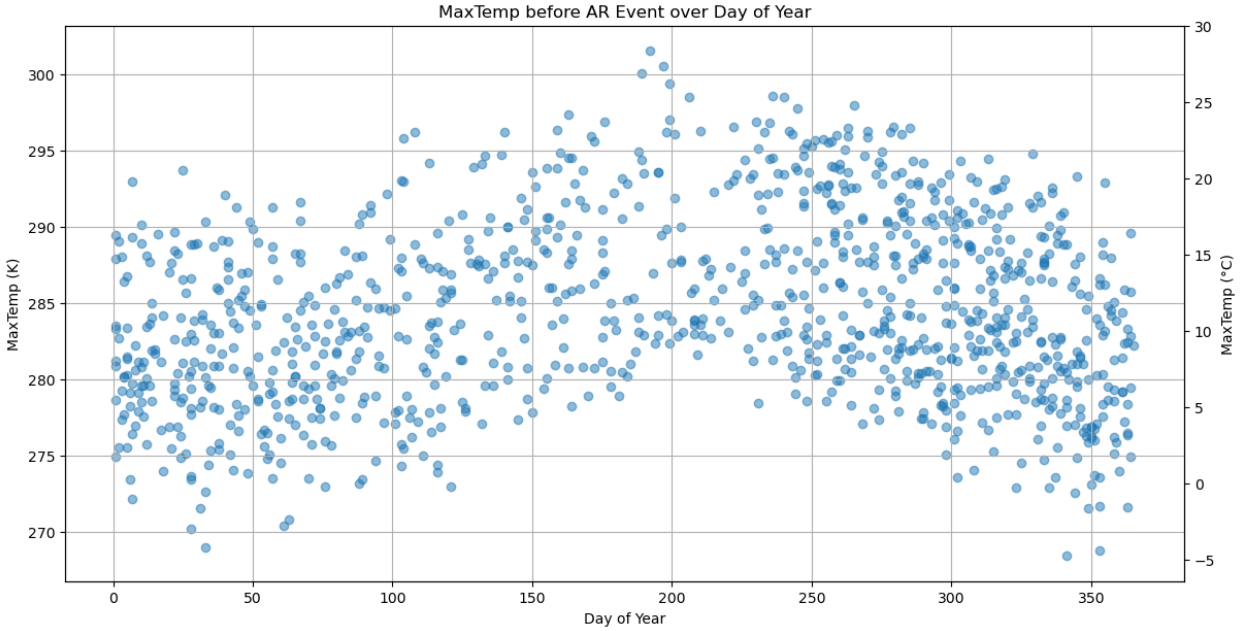

Figure A1. Maximum Pre-landfalling LST Distribution. This is the original version of Figure 7, which shows a clear overall seasonal trend and a high variance of the LST.

APPENDIX B: Hypothesis Test Graphs on Latitude Control

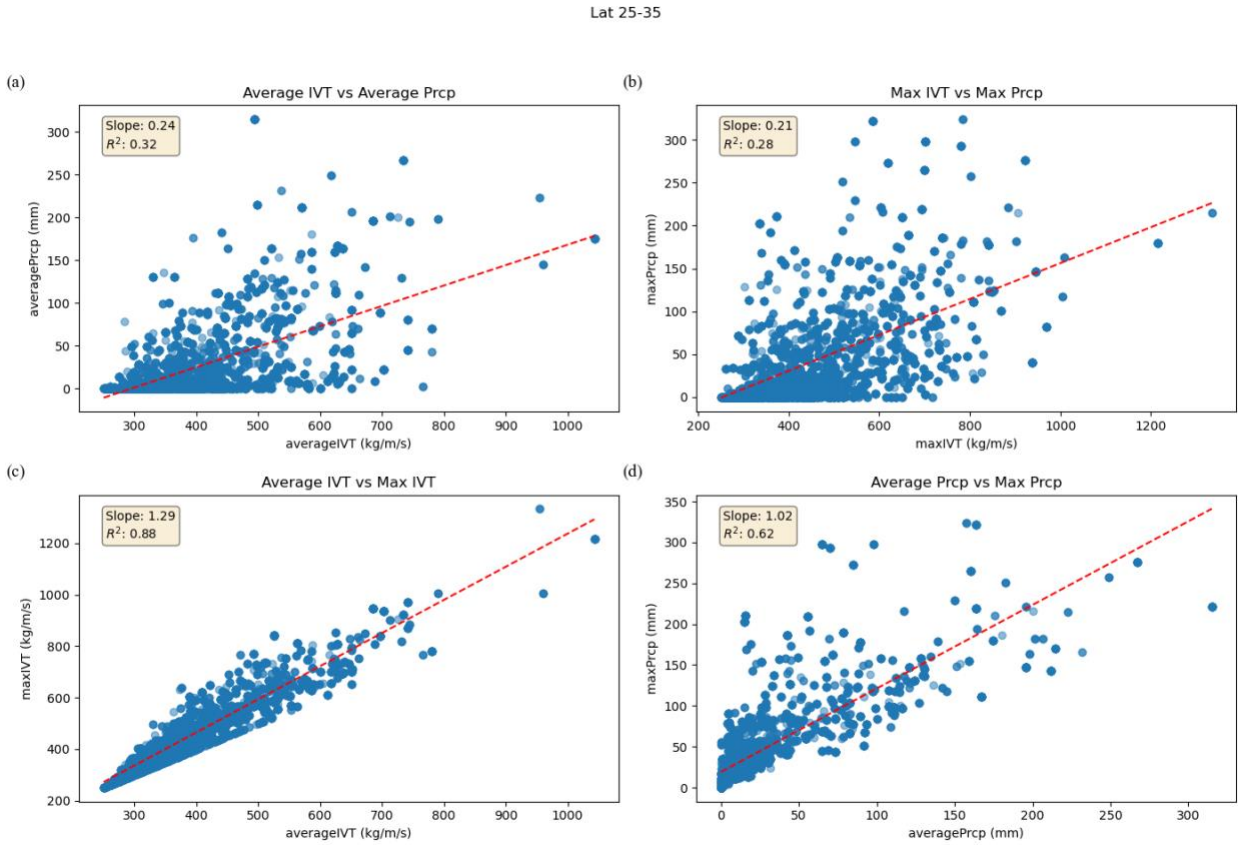

Figure B1. IVT vs. Precipitation Analysis in latitude range 25°N-35°N. Similar to Figure 9, This set of scatter plots explores the relationship between IVT and precipitation intensity for each AR-induced precipitation event within this latitude range, detailing (a) average IVT vs. average precipitation, (b) maximum IVT vs. maximum precipitation, (c) average IVT vs. maximum IVT, and (d) average precipitation vs. maximum precipitation.

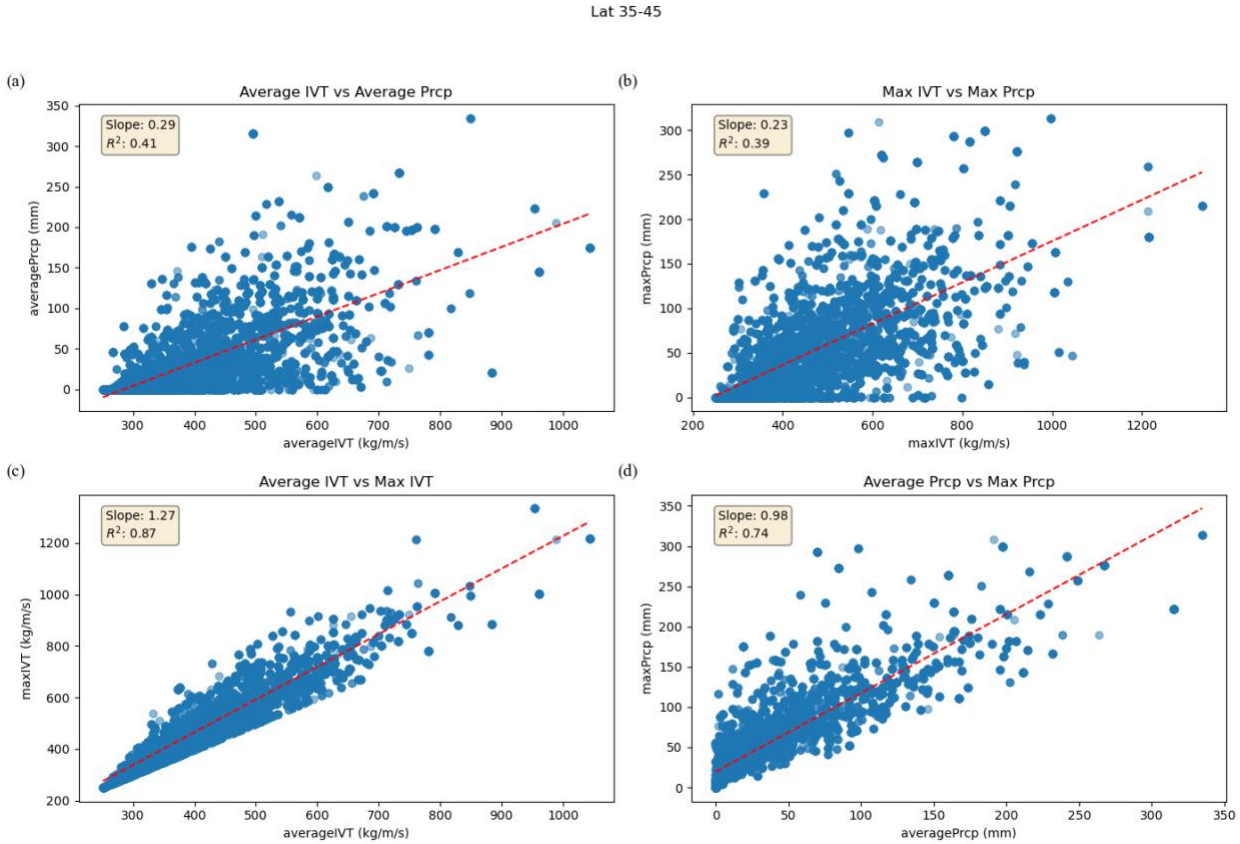

Figure B2. IVT vs. Precipitation Analysis in latitude range 35°N-45°N. Similar to Figure 9, this set of scatter plots investigates the relationships between IVT and precipitation intensity, featuring comparisons of (a) average IVT vs. average precipitation, (b) maximum IVT vs. maximum precipitation, (c) average IVT vs. maximum IVT, and (d) average precipitation vs. maximum precipitation.

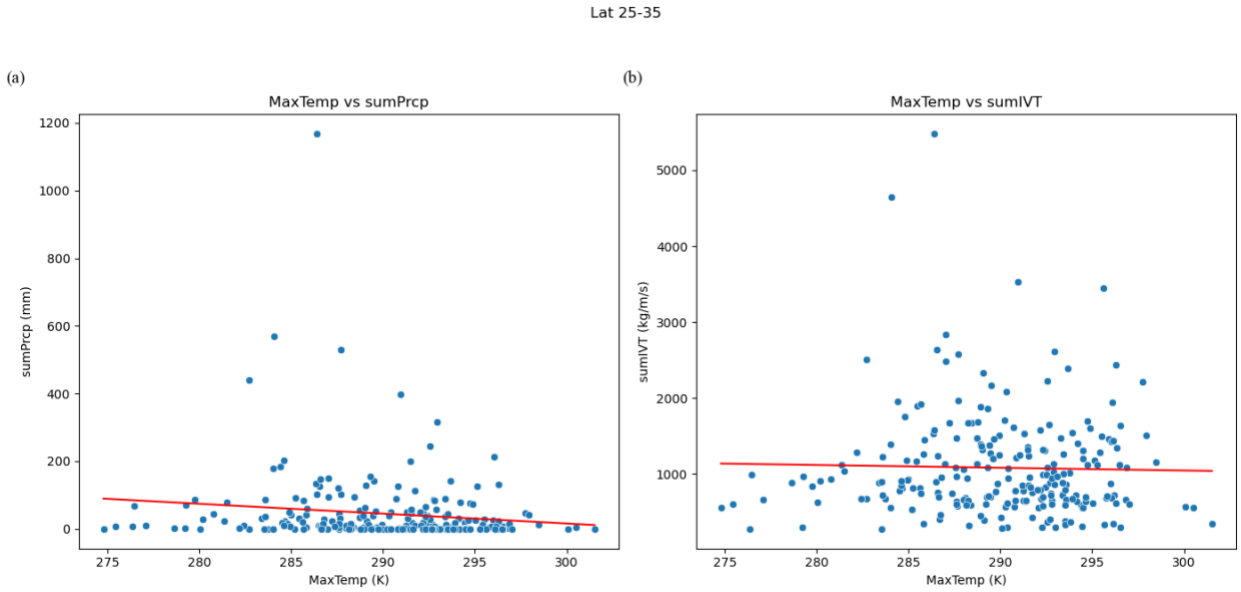

Figure B3. The Interrelationship between LST and AR in latitude range 25°N-35°N. Similar to Figure 10, This scatter plot examines the correlation between pre-landfall LST and AR characteristics such as (a) cumulative precipitation and (b) cumulative IVT within this specific latitude range.

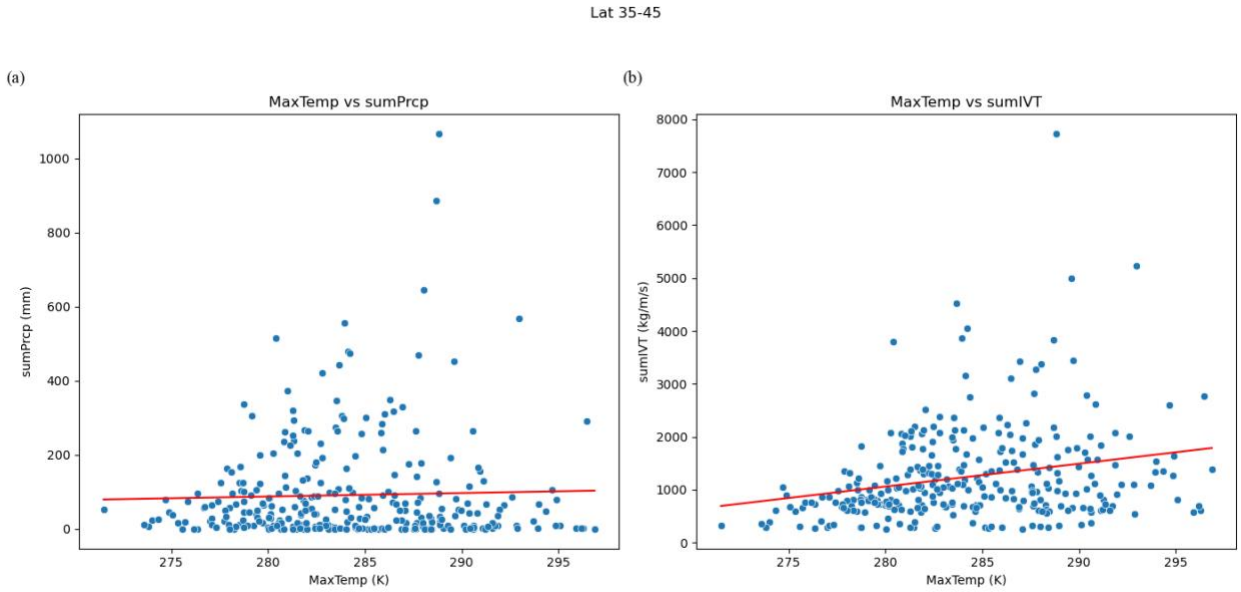

Figure B4. The Interrelationship between LST and AR in latitude range 35°N-45°N. Similar to Figure 10, this plot analyzes the correlation between LST prior to AR landfall and AR outcomes including cumulative precipitation and IVT for this latitude band.

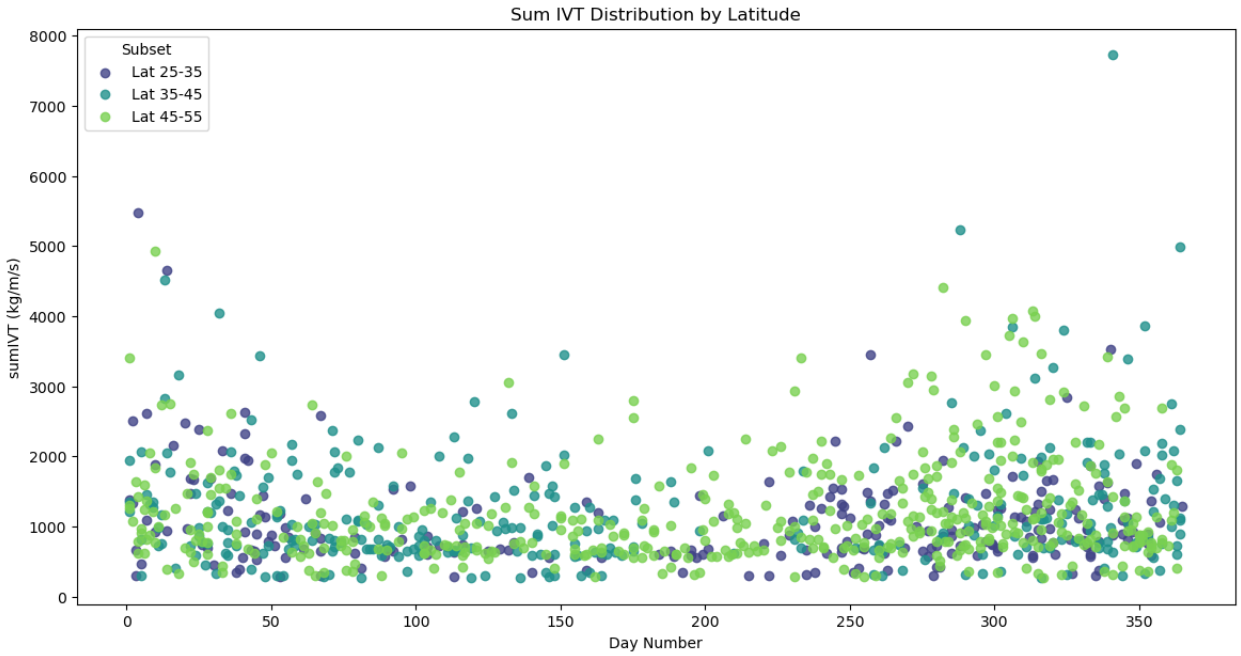

Figure B5. Total IVT Distribution under Latitude Control. This graph displays the total integrated water vapor transport (IVT) for each AR event plotted across different days of the year, with color coding to indicate different latitude zones, highlighting the spatial variability of IVT.

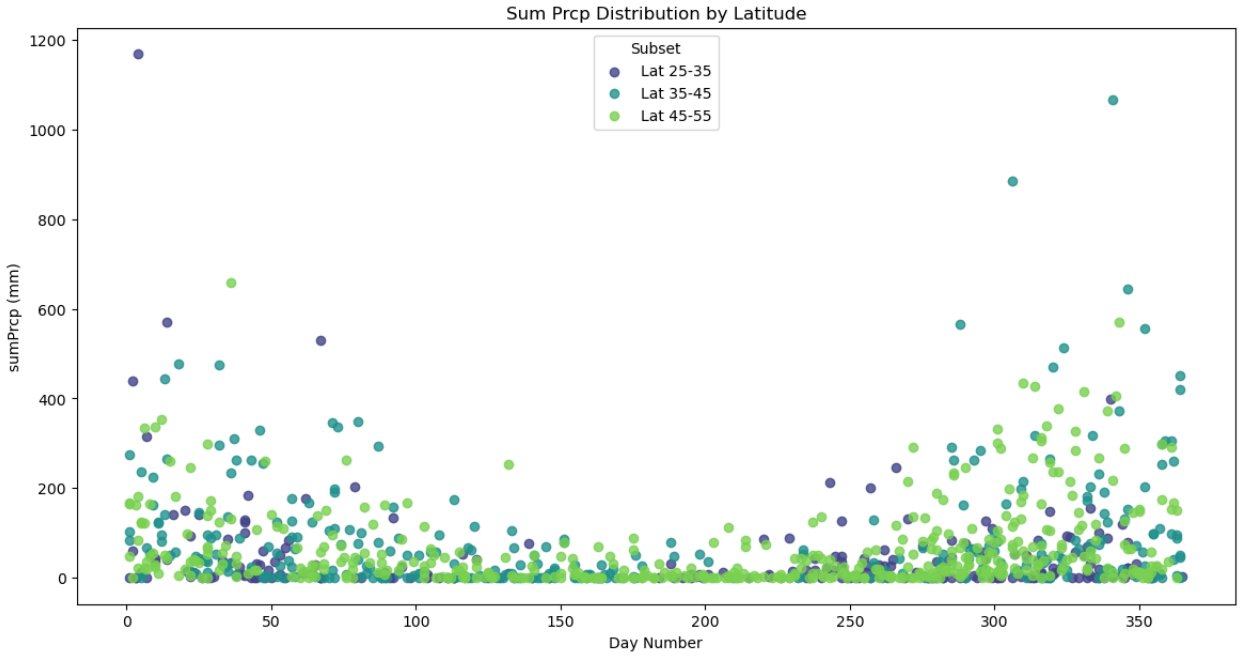

Figure B6. Total Precipitation Distribution under Latitude Control. This plot shows the total precipitation for each AR event across the year, with variations in the size and color of the dots to illustrate the intensity and frequency of precipitation events in different latitude zones.

APPENDIX C: Relavent Graphs for Context Understanding

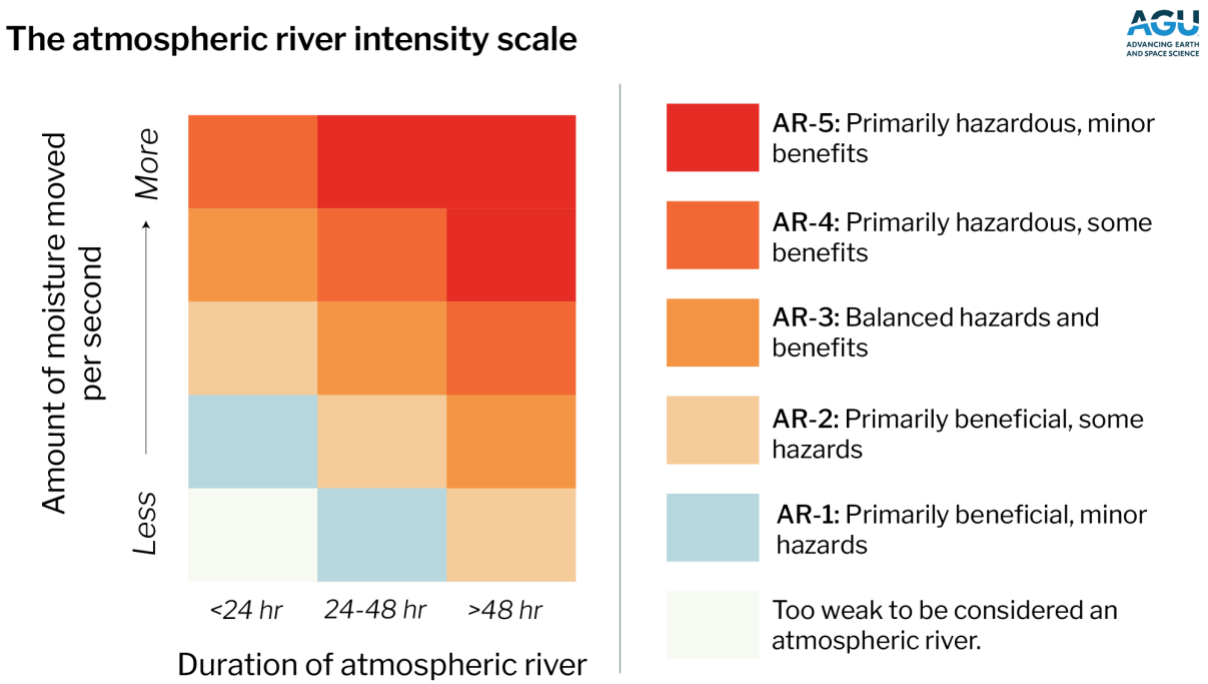

Figure C1. AR Intensity Scaling. This graph illustrates the strength of atmospheric rivers based on their duration, typically ranging from 24 to 72 hours, and the volume of moisture they transport, measured in kilograms per meter per second along the vertical axis (Ralph et al. 2019).